University of Maryland College Park
Department of Chemistry and Biochemistry

Mass and Charge Distributions in Fe-Induced Reactions

H. Madani, A.C. Mignerey, A.A. Marchetti, A.P. Weston-Dawkes,
W.L. Kehoe, and F. Obenshain

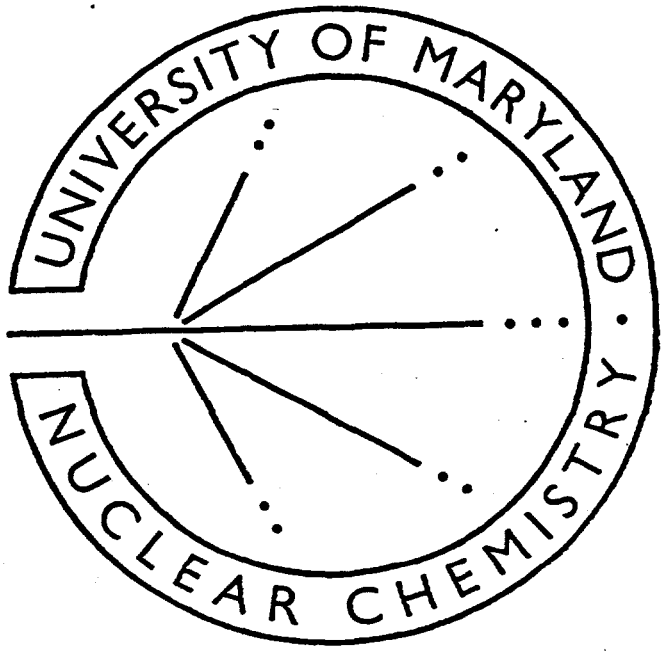

DOE/ER/40802-2

February 21, 1995

University of Maryland College Park
Department of Chemistry and Biochemistry

Mass and Charge Distributions in Fe-Induced Reactions

H. Madani, A.C. Mignerey, A.A. Marchetti, A.P. Weston-Dawkes,
W.L. Kehoe, and F. Obenshain

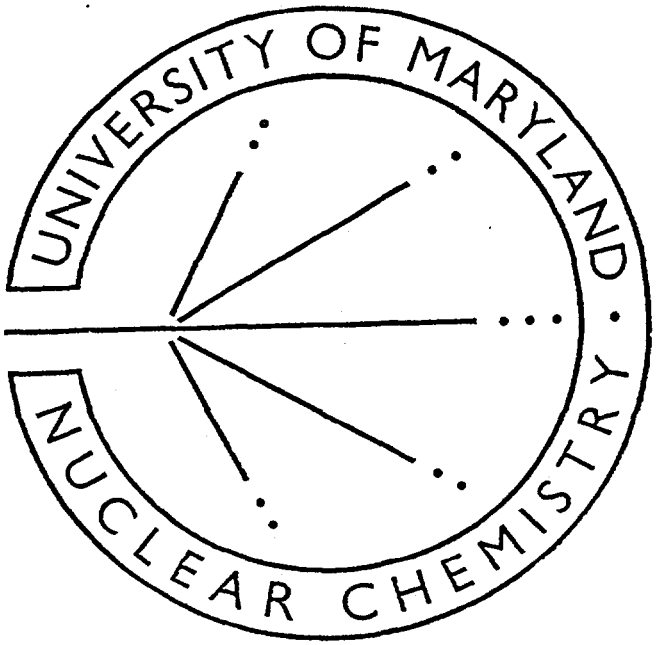

DOE/ER/40802-2 February 21, 1995

DISCLAIMER

Mass and Charge Distributions in Fe-Induced Reactions

H. Madani, A.C. Mignerey, A.A. Marchetti*, A.P. Weston-Dawkes†, W.L. Kehoe‡

University of Maryland, College Park, Md 20742

F. Obenshain

Oak Ridge National Laboratory, Oak Ridge, Tennessee 37831

February 24, 1995

Abstract

The charge and mass of the projectile-like fragments produced in the 12-MeV/nucleon ^{56}Fe + ^{165}Ho reaction were measured at a laboratory scattering angle of 16 degrees. The mass and charge distributions of the projectile-like fragments were generated as a function of total kinetic energy loss (TKEL), and characterized by their neutron and proton centroids and variances, and correlation factors. A weak drift of the system towards mass asymmetry, opposite to the direction which minimizes the potential energy of the composite system, was observed. The increase in the variances with energy loss is consistent with a nucleon exchange mechanism as a means for energy dissipation. Predictions of two nucleon exchange models, Randrup's

---

*Lawrence Livermore National Laboratory, Livermore, California 94550.

†Washington, DC 20585

‡Brookhaven National Laboratory, Upton, New York 11973

and Tassan-Got's models, are compared to the experimental results of the 672-MeV $^{56}Fe + {}^{165}Ho$ reaction and to other Fe-induced reactions. The proton and neutron centroids were found to be generally better reproduced by Tassan-Got's model than by Randrup's model. The variances and correlation factor are well reproduced for asymmetric systems by both models.

PACS number(s): 25.70.Lm

1. INTRODUCTION

Extensive studies of heavy-ion induced reactions in the deep-inelastic region have resulted in the understanding of their general features[1–5]. At low bombarding energies (a few MeV/nucleon above the Coulomb barrier), the system remains binary and the two fragments emerging from the collision carry all the nucleons of the system. Large amounts of relative kinetic energy and angular momentum are converted into excitation energy and intrinsic spin of the two fragments, which subsequently decay via particle evaporation, gamma emission, and/or fission. The experimentally observed broadening of the mass and charge distributions with increasing total kinetic energy loss (TKEL) is indicative of nucleon transfer between the two reaction fragments. However, there is yet little evidence whether nucleon transfer alone can account for all the excitation energy produced in deep-inelastic reactions. Furthermore, how this excitation energy is shared between the projectile-like fragment (PLF) and the target-like fragment (TLF) is still an open question[6–10]which will be addressed in a subsequent paper.

Another aspect of deep-inelastic reactions which has yielded conflicting results is the strong drift towards mass asymmetry observed in many asymmetric systems. Such a drift is counter to the direction that minimizes the static potential energy of the composite system[11]. The study of the 887-MeV ^{58}Ni on ^{197}Au by Awes *et al.*[12] resulted in an agreement between the data and the predictions of the potential energy surface (PES) gradient only if equal

excitation energy division between the reaction fragments was assumed. On the other hand, experiments with ^{58}Ni and ^{64}Ni on ^{238}U at 8.3 MeV/nucleon by Breuer *et al.*[13], ^{74}Ge on ^{165}Ho at 8.3 MeV/nucleon by Planeta *et al.* and Kwiatkovski *et al.*[11,7], and ^{56}Fe on ^{165}Ho at 9 MeV/nucleon by Benton *et al.*[6,14] showed that the experimental data do not always follow the direction predicted by the PES gradient[11]. Except for the ^{74}Ge on ^{165}Ho system, the predominant feature observed was the increase in neutron number and decrease in proton number, resulting in the production of neutron-rich PLF's and systems that are more asymmetric than that of the entrance channel.

Several models have been proposed to describe the deep-inelastic mechanism. The focus in the present study is on two of these models, Randrup's model[15], and Tassan-Got's model[16,17], each based on stochastic nucleon exchange between the reaction partners. A number of authors have compared the predictions of Randrup's model to experimental results[11,16–20,8]. While the experimental variances are generally well reproduced by the model, the mass and charge centroids are often overpredicted. Randrup's model predicts an evolution towards mass symmetry for asymmetric systems, while experimental data show an opposite trend[11,18,20]. On the other hand, Tassan-Got's model is relatively new and, while it has been compared to only a few systems, it is generally successful in reproducing both the experimental centroids and variances for asymmetric systems[16,18,20].

2. EXPERIMENTAL SETUP

The experiment was performed at the Holifield Heavy Ion Research Facility at Oak Ridge National laboratory. A 672-MeV ^{56}Fe beam was used to bombard a 195-μg/cm^2 ^{165}Ho target with 50 μg/cm^2 of carbon backing. The target was positioned so that the carbon backing was facing the beam. The beam current was between 20 and 40 nA throughout the experiment.

A time-of-flight (TOF) arm, connected to the 30-cm diameter scattering chamber, was used to detect the projectile-like fragments (PLF's) and determine their velocity by measuring their time-of-flight. The TOF arm was positioned at a laboratory angle of 16° with

respect to the beam throughout most of the experiment. The PLF's entered the time-of-flight arm through an oval aperture of 0.32 cm and 0.64 cm minor and major axes, respectively. The PLF's were detected by a parallel plate avalanche counter (PPAC) mounted in the time-of-flight arm 23 cm behind the TOF aperture. A second PPAC was positioned at 225 cm behind the TOF aperture, resulting in a flight path of 202 cm between the two PPAC's. The PPAC closest to the time-of-flight arm aperture had an active area of 2 cm by 2 cm and was used as a start detector. The second PPAC had an active area of 8 cm by 8.5 cm and was used as a stop detector. Each PPAC was composed of four windows. The two internal ones were used as cathodes and were 50 $\mu g/cm^2$ of polypropylene. The external windows were 40 $\mu g/cm^2$ of aluminized polypropylene. The anode plane of each PPAC was mounted between the two cathodes and was used for time measurement. The second PPAC was also used to provide position, in addition to timing, information. Each cathode of the second PPAC was aluminized with parallel strips spaced 2 mm apart. The metal strips were connected in series via delay chips to outputs at two ends of the cathode plane. The two cathodes were mounted in a configuration where the aluminum strips of one were perpendicular to the strips of the other. Both horizontal (x-left and x-right) and vertical (y-up and y-down) positions could thus be obtained. Both PPAC's were filled with isobutane gas at a pressure of 2.7 torr.

The energy of the projectile-like fragments was measured using a gas ionization chamber located at the end of the time-of-flight arm. The entrance to the gas ionization chamber was a 9.5 cm by 9.5 cm 200-$\mu g/cm^2$ mylar window placed at a distance of 10.5 cm behind the second PPAC. Two horizontal support bars were placed on the window dividing it into three equal sections of 9.5 cm by 3.6 cm each. The gas ionization chamber had four anodes of lengths 10, 10, 20, and 40 cm, respectively, separated by 0.8 cm gaps. Since the anodes were used to measure the kinetic energy deposited in the gas, they are referred to as the ΔE1, ΔE2, ΔE3, and E4 detectors, respectively. The ionization chamber was filled with tetrafluoromethane (CF_4) at a pressure of 105 torr.

The absolute energy calibration was performed using elastic events. The STOPX pro-

gram from Oak Ridge[21] was used to calculate energy losses in half of the target and in the various windows and gas media that the projectile-like fragments traverse before entering the gas ionization chamber. These were subtracted from the calculated elastic kinetic energy before performing the final absolute calibration.

Contour maps of the PLF laboratory energy versus the PPAC derived x- and y-positions showed a dependence of the energy upon the horizontal (x) position but almost none on the vertical (y) position. After correcting the position dependence with a third degree polynomial, the energy resolution obtained was estimated to be 1.2% full width at half maximum (FWHM) for the elastic peak.

The projectile-like fragment charge was determined with the ΔE-E method. The sum of the calibrated energies from the first and second elements of the gas ionization chamber served as the ΔE, and was plotted versus the total kinetic energy E (sum of all four elements of the ionization chamber) to result in Z lines which were straightened empirically by the use of polynomials.

Discontinuities in the Z lines were observed at total kinetic energy values corresponding to the gap between the ΔE3 and E4 anodes of the gas ionization chamber. These discontinuities were attributed to different efficiencies of charge collection by the anodes in the gap region. This effect is expected at all regions of the ΔE-E plane corresponding to gaps between anodes. However, since a large fraction of the PLF's lose most of their energy in the ΔE3 and E4 detectors, the effect of the gap between ΔE3 and E4 is magnified. Hence, different polynomials were used for the two different regions of the ΔE-E plane that were created by the discontinuity between ΔE3 and E4. The empirical corrections resulted in straight lines corresponding to discrete atomic numbers separated by one unit of charge. The charge resolution was estimated to be 0.3 charge units. Histograms of calibrated charge were generated for energy gates spanning the entire energy range to monitor the variation of the charge centroids with energy and to ensure that the range of variation of the Z centroids with energy was within the accepted range of 0.1 units of charge.

The time-of-flight of the projectile-like fragments was used for their mass number de-

termination. The measured time-of-flight included an offset T_0 which accounted for the delay between the start and stop signals due to the electronics. This was included in the calibration by defining a new time-of-flight as

$$TOF = TOF_{measured} - T_0 \quad (1)$$

The value of T_0 was determined by trial and error to minimize the dependence of the mass number on energy. A two-dimensional spectrum of mass number versus energy was generated for different values of T_0, until the slope of the mass number versus energy curve was the closest possible to zero. Good mass number separation depends on both energy and time-of-flight resolutions. The resolution of the time-of-flight obtained after calibration was 450 ps. A correction similar to the one used to eliminate the dependency of energy on position was also needed for the time-of-flight. The resolution obtained for the time-of-flight was about 380 ps after application of the position correction.

The mass number resolution should be 0.9 mass units at most for identification of the different isotopes. A discontinuity in the mass number lines was observed at energies corresponding to the gap between the ΔE3 and E4 detectors. It was attributed to the same effect observed in the Z spectra . Empirical corrections using polynomials were made to eliminate the discontinuity and to make the mass numbers assignments. The isotopic distributions of each element were then generated individually and the dependence of the mass parameter on energy was corrected with polynomials. The mass resolution obtained with our detection system was about 0.9 mass units. For mass spectra with worst-case resolution, isotopic identification was ambiguous. Therefore, a deconvolution method was utilized to enhance mass separation. This procedure, which is generally used in optical spectroscopy to improve peak separation, was previously investigated by our group and proved successful in the determination of the mass distributions of ^{35}Cl on ^{209}Bi at 15 MeV/nucleon[18,22]. Detailed information about the deconvolution technique can be found in Ref.[22] and references therein.

The deconvolution procedure mainly consisted of smoothing the data to improve the

signal to noise ratio, and deconvolving the smoothed spectra. It should be emphasized that the deconvolved spectra (when necessary) were used only in the determination of the various polynomials that describe the energy dependence of the mass parameter and for absolute mass calibration. All the data analyses were otherwise performed on an event-by-event basis.

3. DATA REDUCTION

The amount of kinetic energy converted into forming the reaction products in their ground states (Q_{gg}), plus the individual fragment excitation energies, is referred to as the total kinetic energy loss (TKEL) and is equivalent to the Q of the reaction. It is defined as the difference between the total kinetic energy before the reaction and the total kinetic energy (TKE) after the collision. The total excitation energy of the system E^* is

$$E^* = TKEL + Q_{gg}, \tag{2}$$

where Q_{gg} is the ground state Q-value. Corrections for the binding energy and the kinetic energy of the particles evaporated prior to fragment detection were made using an iterative procedure that used results from the evaporation code PACE II[23]. This code simulates the statistical emission of neutrons, protons, alpha particles and gamma rays by a Monte Carlo technique. It had been shown in earlier studies of heavy-ion collisions[12,24,9] that there is a satisfactory agreement between experimental data and PACE II predictions in the range of excitation energies obtained with the reactions used in the present study.

Among the inputs to the PACE program are the angular momentum of the PLF and its excitation energy. The angular momentum or spin of the PLF was determined using the assumption of the sticking limit[6]. However, evaporation calculations with different values for the nuclear spin have shown that the amounts of mass and charge evaporated are not, on the average, strongly dependent on spin, for the range of values (2 to 15$\hbar$ units) obtained from the 672-MeV ^{56}Fe on ^{165}Ho reaction[6,18]. Therefore, only the initial spin of the primary PLF was used for the entire excitation energy range.

Two possibilities were considered for the excitation energy parameter: 1) an equal sharing of the total available excitation energy E^*_{TOT} by the PLF and the TLF and 2) a statistical equilibrium between the two fragments, which thus have equal nuclear temperatures. In this latter case, E^*_{TOT} is divided between the reaction fragments in proportion to their mass numbers. To obtain the amount of evaporated mass as a function of excitation energy, a range of excitation energies extending from 0.25 to 2 MeV/nucleon was used in steps of 0.25 MeV/nucleon. For each step, evaporation corrections were applied to a range of nuclei with mass and atomic numbers chosen to yield, after evaporation, a distribution of nuclides whose N/Z ratio is between the N/Z ratio of the projectile and that of the compound nucleus. The functional forms of the evaporated mass, in terms of available excitation energy, were determined by linear fits. The iteration procedure described in Refs.[18,9] was then employed to compute a new corrected value for TKEL.

4. EXPERIMENTAL MASS AND CHARGE DISTRIBUTIONS

The mass and charge distributions of the projectile-like fragments from the 672-MeV ^{56}Fe on ^{165}Ho reaction were determined by moment analysis. Contour plots of Z versus N were generated for different gates of TKEL. Examples of these plots are displayed in Figure 1. In a moment analysis method, the charge centroids (first moments), <Z>, and variances (second moments), σ_Z^2, are expressed by the equations

$$<Z> = \frac{\sum_{i=1}^{n} Z_i}{n} \tag{3}$$

and

$$\sigma_Z^2 = \frac{\sum_{i=1}^{n}(Z_i - < Z >)^2}{n-1}. \tag{4}$$

Analogous equations are used for the neutron centroids and variances. The correlation factor, ρ_{NZ}, is given by

$$\rho_{NZ} = \frac{\sigma_{NZ}}{\sigma_N \sigma_Z} \tag{5}$$

where σ_{NZ} is the covariance and is written as

$$\sigma_{NZ} = \frac{\sum_{i=1}^{n}(Z_i - < Z >)(N_i - < N >)}{n-1} \tag{6}$$

If the distributions were pure Gaussians these would be equivalent to the distribution centroids and variances, respectively, in a Gaussian formulation. When the distributions deviate from pure Gaussian shapes, the centroids obtained by performing two-dimensional Gaussian fits on the distributions or by using the methods of moments are not significantly different. However, in such cases the variances determined by moment analysis tend to be greater than those obtained by Gaussian fits[18]. When the distributions do not depart considerably from Gaussian shapes, the two approaches yield similar values for the centroids and variances[18].

The moment analysis method was used in this study to determine the neutron and charge centroids, the <N>/<Z> ratio, the variances σ_Z^2 and σ_N^2, and the correlation factor ρ_{NZ} for the PLF neutron and charge distributions for consecutive bins of TKEL. Bins of 10 MeV were used for TKEL values smaller than 100 MeV. For TKEL values between 100 MeV and 240 MeV, 20 MeV energy loss bins were used. Above a TKEL value of 240 MeV, where the number of events is low, bins of 40 MeV of energy loss were applied. The results obtained for the centroids and variances using the equal excitation energy division assumption are summarized in Tables 1 and 2, and in Figures 2 and 3. The error bars on the experimental data shown in these plots were calculated by the method of statistical error propagation in the formulas of the first and second moments of the distributions and are smaller than the symbol. Comparisons between the results obtained with the two assumptions for the division of the excitation energy showed only a slight difference for the centroids and the variances at TKEL values higher than 360 MeV, where the centroids and widths obtained with the thermal equilibrium assumption are slightly higher. No difference was observed at lower TKEL values[9]. Evaporation corrections of the energy loss scale do not seem to cause a noticeable effect on the behavior of the distributions with TKEL, especially in the range of energy damping below the entrance channel (312 MeV). Therefore, only the results obtained

using the assumption of equal partition of the excitation energy are reported here, unless otherwise specified.

As shown in Figure 2, the charge centroids decrease steadily with increasing energy loss. The neutron centroids decrease gradually with increasing TKEL; this decrease is less pronounced during the first 100 MeV of TKEL. A steeper slope is observed for TKEL values above 300 MeV for both <N> and <Z>. The <N>/<Z> ratio remains essentially constant and equal to the N/Z ratio of the projectile for most of the TKEL range. A decrease in <N>/<Z> is observed above 300 MeV of TKEL. The arrows displayed in these plots indicate the TKEL corresponding to the entrance channel Coulomb barrier, which is 312 MeV for the 672-MeV ^{56}Fe on ^{165}Ho system. This merely serves as a guide since in the region of fully damped events a lowering of the Coulomb barrier is expected from the formation of asymmetric and deformed products. In addition, decay via sequential break-up as opposed to particle evaporation may be possible.

The variances σ_Z^2 and σ_N^2 and the correlation factor ρ_{NZ} are plotted as a function of TKEL in Figure 3. Both variances increase with increasing TKEL. They reach a maximum value at about 340 MeV of energy loss, which is around the same value where the slope of the centroids and the <N>/<Z> ratio changes, then start decreasing. The neutron variance values are higher than those of the proton variance for the whole range of energy loss. The correlation factor ρ_{NZ} raises rapidly from -0.3 at 5 MeV of TKEL to about 0.65 at 100 MeV of TKEL. Above 100 MeV, ρ_{NZ} continues to increase with increasing TKEL, but at a slower rate, and reaches values close to 1, which indicates a strong correlation between neutron and proton transfer, at 300 MeV of TKEL.

An estimate of the mass of the primary PLF, A'_{PLF}, was made by adding the amount of evaporated mass computed with PACE II to the measured post-evaporation PLF mass. Charge evaporation was assumed to be negligible, based on studies which have shown that most of the contribution to the evaporated mass in this system is from neutrons[13,25,26]. The primary PLF neutron number is thus determined by subtracting the measured PLF charge from the primary PLF mass. The centroids $< N'_{PLF} >$ of the primary PLF neutron

distribution obtained are summarized in Table 3 and displayed in Figure 4 as a function of TKEL. The value of $< N'_{PLF} >$ increases with increasing TKEL and reaches a maximum at a TKEL value close to the limit determined by the entrance channel Coulomb barrier, which is indicated by the arrow.

5. MODEL CALCULATIONS

Several models based on different approaches have been developed to describe the mechanisms involved in the system evolution towards equilibrium in deep-inelastic reactions. Experimental evidence, such as the broadening of the charge and mass distributions of the detected fragments with increasing total kinetic energy loss, supports the hypothesis of energy damping by means of nucleon transfer between the primary fragments of a heavy-ion reaction in the deep-inelastic region. Therefore, it is possible to describe the process occurring in deep-inelastic collisions in terms of transport phenomena, as is the case in both Randrup's model[15] and Tassan-Got's model[16,17]. The physical picture of the reaction is the same in both treatments. The two nuclei are approximated by two spheres that approach each other along Coulomb trajectories until they are within the range of the nuclear field. A stochastic exchange of nucleons between the two interacting partners occurs through a cylindrical neck and leads to the transport of mass, charge, energy and angular momentum. This nucleon transfer is assumed to be the only source of energy dissipation. However, two different approaches and some different basic assumptions are used by the two authors in their determination of the variables of the system. A brief description of the two models follows. More detailed discussions can be found in Refs.[15–17].

In Tassan-Got's model calculations the stochastic transfer of nucleons between the two fragments is simulated by a Monte Carlo method. In this approach, the direction and type of transfer are decided by random drawing. The relative motion is described in terms of time, distance, and angle increments. A transfer occurs if the transfer time, Δt_{tr}, which is generated by random drawing, is smaller than the aforementioned time increment. The

transition probabilities of a proton or a neutron out of or into a fragment are calculated and used for the determination of the characteristics of each transfer. A phase-space formula accounting for Pauli blocking is used by Tassan-Got to evaluate these transfer probabilities.

A nucleon transfer results in the modification of the initial conditions of the relative motion, which are readjusted before the next transfer. This procedure is repeated until the two nuclei are too far apart to be influenced by the nuclear potential. They then depart from each other along Coulomb trajectories. The values of the macroscopic variables of interest are determined event-by-event and stored. Calculations are performed for a wide range of impact parameters to include all possible incident waves.

In Randrup's approach the relative motion of the dinuclear system is determined using a mean trajectory approximation. The dynamical variables of the system, which include the proton and neutron numbers of the PLF's, the radius of the small cylindrical neck that joins the two interacting ions, and the mean spin projection for the projectile-like and target-like fragments, follow the Lagrange-Rayleigh equations of motion

$$[\frac{d}{dt}\frac{\partial}{\partial \dot{\overline{q_i}}} - \frac{\partial}{\partial \overline{q_i}}]L = -\frac{\partial}{\partial \dot{\overline{q_i}}}F \tag{7}$$

where $\overline{q_i}$ and $\dot{\overline{q_i}}$ are the average values of the macroscopic coordinates and velocities which describe the dinuclear system. The Rayleigh dissipation function F describes the conversion of kinetic energy of the system into excitation energy via nucleon exchange. The potential energy V entering in the formulation of the Lagrangian L, is written as

$$V = V_C + V_N + V_P^{LD} + V_T^{LD} - V_0 \tag{8}$$

where V_C is the Coulomb potential, V_N is the nuclear interaction potential, V_P^{LD}, and V_T^{LD} are liquid-drop binding energies for the projectile-like fragment and the target-like fragment, respectively, and V_0 is a normalization constant. The Fermi levels that govern the evolution of the system are extracted from the Lagrangian of the system. It is argued by Tassan-Got that this causes the system to drift towards symmetry, and that this effect is due to the presence of a kinetic term in the Lagrangian[16,17].

The fluctuations around the average values of these coordinates are described by the Fokker-Planck equation:

$$\frac{\partial P(A,t)}{\partial t} = -\sum_{\alpha} \frac{\partial}{\partial C_\alpha} V_{C_\alpha} P(A,t) + \sum_{\alpha,\beta} \frac{\partial^2}{\partial C_\alpha \partial C_\beta} D_{C_\alpha C_\beta} P(A,t), \tag{9}$$

where P(A,t) is the probability of finding one of the reaction partners (the PLF for instance) in state A at time t, C_α and C_β are variables that describe the system's charge and neutron numbers, and V_{C_α} and $D_{C_\alpha C_\beta}$ are the drift and diffusion coefficients, respectively. The drift coefficient governs the evolution of the mean values of the macroscopic variables C, and the diffusion coefficient governs the evolution of their variances.

Equation 9 is solved by the determination of the transport coefficients V_{C_α} and $D_{C_\alpha C_\beta}$. In Randrup's approach they are evaluated by considering the dinuclear system as two Fermi-Dirac gases which interact by exchanging particles. Time-dependent perturbation theory is utilized, with the observables represented by one-body operators. More details about the calculation of the transport coefficients for transport of mass, energy and angular momentum can be found in Ref. 12.

6. COMPARISON BETWEEN THE TWO MODELS AND THEIR PREDICTIONS

Some of the basic differences between Randrup's and Tassan-Got's model calculations include the way the Fermi levels are calculated in each approach, and the restriction on the direction of transfer in Tassan-Got's formulation. In Randrup's model the Fermi levels are extracted from the Lagrangian, while in Tassan-Got's model the Fermi levels are determined for each nucleus independently as separation energies calculated from mass tables. This is thought to be one of the crucial factors that causes the differences between the predictions of the two models for asymmetric systems. It seems that the presence of a kinetic term in the Lagrangian used in Randrup's model leads the system to drift towards mass symmetry[16,17]. In Tassan-Got's model the mass and charge drifts are insensitive to relative kinetic energy. Finally, nucleon transfers in Tassan-Got's model are restricted to those where nucleons move

towards the window. There are no restrictions on the direction of transfer in Randrup's model.

A. Primary Distributions

The evolution with TKEL of the centroids, variances, and correlation factor of the nuclide distribution predicted by the two model calculations for the PLF's emitted in the 672-MeV ^{56}Fe on ^{165}Ho and 840-MeV ^{56}Fe on ^{238}U reactions are compared to experimental data in Figures 5 and 6. In both figures the values of $< N >$, $< Z >$, $< N > / < Z >$, σ_Z^2, σ_N^2, and ρ_{NZ} predicted by Randrup's model calculations are indicated by the solid lines before evaporation correction and by the dotted lines after evaporation correction. Similarly, Tassan-Got's model calculations are indicated by the dashed and dot-dashed lines for results before and after evaporation correction, respectively.

For the 672-MeV ^{56}Fe on ^{165}Ho system, the primary neutron centroids obtained using Tassan-Got's model calculations are nearly constant while the primary charge centroids decrease with increasing energy dissipation for TKEL values less than 240 MeV. Above 240 MeV the $< Z >$ and $< N >$ decrease with a relatively steep slope. On the other hand, Randrup's model calculations predict a quite different trend. For TKEL values less than 280 MeV, the primary neutron centroids increase with increasing TKEL, while the primary charge centroids remain nearly constant. Above 280 MeV of TKEL both $< N >$ and $< Z >$ start decreasing. These distinctly different behaviors of $< N >$ and $< Z >$ predicted by the two models result in the same quantitative trend for the $< N > / < Z >$ ratio, which increases from the N/Z of the projectile at low TKEL towards the N/Z of the composite system at higher TKEL. This trend of the centroids $< Z >$ and $< N >$ indicates that in Randrup's model the system evolves towards mass symmetry, while in Tassan-Got's model the system tends to become more asymmetric with increasing energy loss.

The primary variances σ_Z^2 and σ_N^2 from both models are in good agreement for values lower than about 240 MeV of TKEL. At this point, the values from Tassan-Got's model

start decreasing while those from Randrup's model increase with a steeper slope. This effect was also observed in the study of the ^{35}Cl on ^{209}Bi reaction at 270 MeV and the ^{37}Cl on ^{209}Bi reaction at 529 MeV by Marchetti *et al.*[18] A possible explanation for this difference in the behavior is the restriction in Tassan-Got's model of nucleon transfers to only the nucleons moving towards the neck of the dinuclear system.

The <N> and <Z> predicted for the 840-MeV ^{56}Fe on ^{238}U system exhibit the same trend as for the previous system. However, the difference between the centroids from the two models, the neutron centroids in particular, is larger for this more asymmetric system. Up to 9 neutrons are transferred from the TLF to the PLF in Randrup's approach and there is a gain of about 2 charge units by the PLF. Tassan-Got's model predicts that a maximum of 7.4 charge units are transferred from the PLF to the TLF. The PLF immediately gains 1 neutron then remains nearly constant until 360 MeV of TKEL. Above 360 MeV of TKEL the PLF loses up to 3 neutrons. Both models predict essentially the same <N>/<Z> ratio for this system. The <N>/<Z> ratio increases from the N/Z of the projectile at 0 TKEL to close to the N/Z of the composite system at the TKEL limit imposed by the entrance channel Coulomb barrier (indicated by the arrows).

A small difference between the predictions of the two models is observed for the variances obtained for the 840-MeV ^{56}Fe on ^{238}U system. Tassan-Got's model generally predicts a smaller σ_Z^2. The correlation factor evolves from no correlation (ρ_{NZ}=0) at the first stages of the collision (low TKEL) towards strong correlation ($\rho_{NZ} \approx 1$) at the later stages (higher TKEL) for both calculations.

B. Excitation Energy Derivation and Evaporation Calculations

The observables measured during experiments are secondary quantities which describe the system after it has lost all its excitation energy by evaporation of light particles, gamma ray emission, and/or fission. It is therefore essential to account for the loss in proton and neutron numbers by evaporation before attempting any comparisons of model predictions

to experimental data. Two possibilities exist for making such corrections. One is to add evaporated charge and mass evaluated from evaporation codes to the measured secondary values. However, because it is not easy to determine how much evaporated mass is due to evaporation of protons or neutrons, reliable results are obtained only in cases where neutron evaporation is much more significant than proton evaporation. The other method is to perform evaporation calculations on the primary distributions predicted by the models and compare these derived secondary distributions to the experimental distributions. This procedure was employed in the present analysis. The evaporation code PACE II[23] was used to account for evaporation of the primary distributions obtained from both models.

In Randrup's model, the average values of the observables considered (charge and neutron number for instance) are calculated. It was therefore necessary to generate two dimensional Gaussian distributions to be used with PACE II by employing the averages <Z> and <N>, the variances σ_Z^2 and σ_N^2, and the covariance σ_{NZ} obtained using Randrup's code. Another input to the evaporation code is the excitation energy of the primary fragment. In the case of Randrup's model, this quantity can be determined using the average rotational energy and the temperatures of the PLF and TLF obtained from Randrup's code. The total thermal energy ($E_{PLF}^{thermal} + E_{TLF}^{thermal}$) of a given exit channel is

$$E_{total}^{thermal} = TKEL + Q_{gg} - E_{total}^{rot}, \tag{10}$$

where E_{total}^{rot} is the sum of PLF and TLF rotational energies. The rotational energy of each fragment is obtained by scaling the average rotational energy $< E_{PLF}^{rot} >$ which is given by the code. The general expression of the rotational energy of a nucleus with a moment of inertia I and total angular momentum ℓ is written as

$$E_{PLF}^{rot} = \hbar^2 \frac{\ell(\ell+1)}{2I}. \tag{11}$$

The moment of inertia, in the solid sphere approximation, is proportional to MR^2 , where M is the mass of the nucleus and R is its radius. Assuming the same angular momentum for each nucleus, the rotational energy E_{rot} of each fragment of mass A_{PLF} in a given exit channel is then calculated as

$$E_{rot} =< E_{rot} > [\frac{< A_{PLF} >}{A_{PLF}}]^{5/3} \tag{12}$$

where $< A_{PLF} >$ is the average mass of each fragment obtained from Randrup's code.

The thermal energies of the PLF and TLF are evaluated using the average temperatures calculated by the code for each fragment. The ratio of excitation energies of the two fragments is given by

$$\frac{E^{thermal}_{PLF}}{E^{thermal}_{TLF}} = \frac{a_{PLF}\tau^2_{PLF}}{a_{TLF}\tau^2_{TLF}} \sim \frac{A_{PLF}\tau^2_{PLF}}{A_{TLF}\tau^2_{TLF}} \tag{13}$$

where A_{PLF} and A_{TLF} are the PLF and TLF masses, a_{PLF} and a_{TLF} are their level density parameters, and τ_{PLF} and τ_{PLF} are their corresponding temperatures. The fraction of thermal energy stored in the PLF can thus be obtained and multiplied by the total thermal energy of the system as given in equation (10) to obtain the PLF thermal energy. The PLF rotational energy is added to this thermal energy and the resulting value is the absolute excitation energy of the PLF, which is used in PACE II. In the case of Tassan-Got's code, the PLF's mass, charge, kinetic energy, excitation energy and intrinsic spin were determined event-by-event and stored in files that were subsequently used as inputs to PACE II.

The PLF excitation energy ratios E^*_{PLF}/E^*_{TOT}, obtained from the two models, are compared in Figure 7 for the 672-MeV ^{56}Fe on ^{165}Ho system. Tassan-Got's model predicts that more than half of the excitation energy is stored in the PLF for TKEL values lower than 60 MeV. On the other hand, Randrup's model predicts an equal division of the excitation energy during the first 60 MeV of TKEL. Above this TKEL value, both models predict similar dependences of E^*_{PLF}/E^*_{TOT} on TKEL. The system tends towards a more thermalized state with increasing energy loss. Since the excitation energies predicted by the two models are similar, and since the same evaporation code was used to obtain the secondary events for both models, any discrepancies between the secondary distributions obtained for the two models are attributed to the inherent differences between the models.

C. Comparison of Experimental Results to Model Predictions

The model predictions obtained after evaporation corrections are compared to experimental data in Figures 5 and 6 for the 672-MeV ^{56}Fe on ^{165}Ho system. The values predicted by both models for <N>, <Z>, and <N>/<Z> show a good agreement with the experimental data for most of the TKEL range. The centroid predictions depart from the experimental data at high values of energy loss, 230 MeV for Randrup's model and 280 MeV for Tassan-Got's model. The model calculations are available only for the range of energy loss defined by the spherical entrance channel Coulomb barrier (TKEL = 312 MeV), as indicated by the arrows. The predicted charge variances agree with the data for most of the TKEL range. At TKEL values close to the maximum energy loss, the variances predicted by the two models diverge from each other. The σ_Z^2 values obtained from Randrup's model continue to increase with increasing TKEL and reproduce the qualitative behavior of the experimental data. The σ_Z^2 values predicted by Tassan-Got's model decrease sharply, in contrast with the experimental data. The neutron variances σ_N^2 are underestimated by both models, even at the very early stages of the reaction and exhibit the same behavior as the proton variances at TKEL values larger than 260 MeV. The correlation factor ρ_{NZ} is well reproduced by both models for this asymmetric system.

For the 840-MeV ^{56}Fe on ^{238}U system[27], Figure 5 shows that the experimental centroids $< N >$ and $< Z >$ are reproduced by Tassan-Got's model calculations for the entire range of allowed energy loss, while they are underestimated by Randrup's model calculations. This discrepancy between experimental and calculated centroid values increases gradually with increasing TKEL. The <N>/<Z> ratio is equally well reproduced by the two models. The variances σ_N^2 are fairly well reproduced by the two model calculations for most of the TKEL range, as shown in Figure 6. On the other hand, the values predicted for σ_Z^2 depart from the experimental data for TKEL values larger than 280 MeV. The correlation factor is fairly well reproduced.

7. DISCUSSION

A. Drift Towards Mass Asymmetry

Studies of various asymmetric systems reveal a tendency for most of these systems to drift towards greater mass asymmetry with increasing TKEL. Transfer of protons from the PLF to the TLF is favored, whereas there is almost no net transfer of neutrons. This trend has been found to be roughly correlated with the PES gradient at the injection point, and is consistent with the equilibration of the isospin degree of freedom, as shown by the the behavior of the N/Z ratio.

It is instructive to compare the experimental nuclide distributions in the N-Z plane to the model distributions to further explore the difference between Randrup's approach and Tassan-Got's approach to the nucleon exchange mechanism. The nuclide distributions obtained for the 672-MeV ^{56}Fe on ^{165}Ho and the 840-MeV ^{56}Fe on ^{238}U systems are displayed in Figure 8. The measured secondary values are indicated by the circles. The primary values indicated by the diamonds were derived via a two-body kinematics technique in the case of the 672-MeV ^{56}Fe on ^{165}Ho system[9], while evaporation corrections have been employed in the case of the 840-MeV ^{56}Fe on ^{238}U. The model calculated primary distributions are indicated by the solid line for the predictions using Randrup's approach, and by the dashed line for Tassan-Got's approach. Similarly, the dotted and dot-dashed lines refer to the calculated secondary distributions using Randrup's and Tassan-Got's model calculations, respectively.

The potential of the system formed by the projectile-like and target-like fragments can be calculated using the relation

$$V = V_{PLF}(LD) + V_{TLF}(LD) + V_N + V_L - V_C \tag{14}$$

where V_N, V_L and V_C are the nuclear, centrifugal and Coulomb potentials, respectively. The nuclear potential V_N is calculated using the proximity formula[12]. The liquid drop (LD) model binding energies V_{PLF}(LD) and V_{TLF}(LD) of the PLF and TLF contain shell corrections but no pairing effects, as calculated from Myers[28].

Using equation 14, a potential energy surface (PES) in the N-Z plane is generated, the gradient of which is indicated by the arrow for each system shown in Figure 8.

The measured data for both systems follow the valley of β stability very closely, as indicated in Figure 8. This is not surprising considering the large amount of evaporation. However, the experimentally reconstructed primary distributions obtained with the 672-MeV ^{56}Fe on ^{165}Ho reaction follow the PES gradient rather closely, while the primary distributions obtained with the 840-MeV ^{56}Fe on ^{238}U reaction are visibly lower than the PES gradient. This discrepancy cannot be attributed to the reconstruction method since the assumptions of equal excitation energy division and only neutron evaporation provide an upper limit to the $< N/Z >$ of the derived primaries.

Tassan-Got's model predictions for the primary distributions follow the PES gradient for both systems, while Randrup's predictions tend towards symmetry and are counter to the PES gradient. The secondary distributions follow the valley of β stability for both models. This produces an agreement with the measured secondary distributions.

The drive towards symmetry predicted by Randrup's model is attributed by Tassan-Got to the presence of a kinetic term in Randrup's formulation of the Lagrangian of the system. In Randrup's formulation of the Lagrangian, the two fragments are considered as one entity; this is equivalent to assuming that the two nuclei have lost their individual characteristics. However, this is true only at long interaction times. Conversely, the interacting nuclei are treated as separate entities in Tassan-Got's model, even at the long interaction times when the two fragments are no longer distinguishable. Therefore, a model which would describe the collision with Tassan-Got's approach at short interaction times, and Randrup's approach at longer interaction times would be an interesting option to consider.

Various explanations have been suggested to account for the strong negative drift in asymmetric systems. In a model proposed by Moretto *et al.*[29], a feedback mechanism attributed to the existence of a temperature gradient between the two fragments was explored. The lighter nucleus is hotter and therefore, by assuming that particle fluxes depend strongly on temperature, a net transfer of particles from the lighter to the heavier fragment oc-

curs. Thus, more mass and energy are transferred to the heavier fragment. However, it was shown by Tassan-Got that this does not account for all the discrepancy between model predictions and experimental data[18]. Model calculations were performed by Tassan-Got for the 370-MeV ^{40}Ar on ^{197}Au system with the constraint of thermal equilibrium between the two fragments. The predictions obtained for primary mass and charge distributions were compared to predictions obtained without the thermal equilibrium constraint. No noticeable difference was observed between the two results. Therefore, it could be concluded that a temperature gradient does not significantly affect nucleon transfer.

Griffin *et al.*[30] calculated a non-classical permeation current flowing between the interacting heavy ions from the deeper potential into the shallower one. This was performed by finding the exact numerical solutions to the simple one-dimensional Schrödinger Double Well model. After an extension of these calculations to three dimensions, and since the depth of the neutron potential well decreases with increasing neutron excess (N - Z), the resulting situation was a flow of neutrons from the heavy nucleus, which has a higher (N - Z) value, to the light nucleus. However, these quantal effects cannot be included in the models discussed here because of their classical treatment of the problem. Since the calculations from Tassan-Got's model produce a negative drift towards mass asymmetry even without taking into account the quantal effects described by Griffin *et al.*[16,17], it could be argued that these effects are not necessary to reproduce the observed drift at least in the 672-MeV ^{56}Fe on ^{165}Ho case.

In Tassan-Got's approach the direction of nucleon transfer is dictated by the sign of the difference between the Fermi energies of the two heavy ions[17]. This difference is expressed as

$$\Delta V = e_2 - e_1' - (e_1 - e_2') \tag{15}$$

where e_2 and e_2' are the Fermi energies of the heavier fragment before and after nucleon transfer occurs, respectively. Similarly e_1 and e_1' describe the lighter fragment. For positive values of ΔV, nucleons are transferred to the lighter nucleus and the opposite is true for

negative values of ΔV. An important property of Tassan-Got's model, which is derived from calculations of ΔV, is that the direction of net nucleon transfer is the one that minimizes a quantity equivalent to that of equation (11), but without the centrifugal term[17]. However, Tassan-Got's model predictions fail to reproduce experimental values at high energy damping[16,17]. This is attributed by Tassan-Got to the fact that, at long interaction times, the boundaries between the two fragments become increasingly blurred, and therefore, the system can no longer be considered binary, and the restriction on the direction of nucleon transfer is not valid.

B. Distribution Variances

An interesting feature observed in Figure 6 for the variances σ_Z^2 and σ_N^2 obtained for the 672-MeV ^{56}Fe on ^{165}Ho system is that they reach a maximum at a TKEL value around that defined by the entrance channel Coulomb barrier. This behavior of the variances was previously observed for the 528-MeV ^{35}Cl on ^{209}Bi system by Marchetti *et al.*[18], and for the 600-MeV ^{40}Ca on ^{209}Bi system by Garcia-Solis *et al.*[31]. This feature could be interpreted as a transition to a sequential statistical breakup of the projectile-like products, as was proposed for systems at higher bombarding energies[32]. The decrease in the variances observed with the 672-MeV ^{56}Fe on ^{165}Ho data is consistent with the behavior of the centroids $< N >$ and $< Z >$ which show a steeper decrease in the same TKEL range. It is also intriguing to note that for the 840-MeV ^{56}Fe on ^{165}U system shown in Figure 6, the values of σ_Z^2 and σ_N^2 exhibit a slight decrease around the TKEL value defined by the entrance channel Coulomb barrier then continue decreasing.

In stochastic nucleon exchange mechanisms, the variances of the fragment distributions are a measure of the number of nucleons exchanged between the interacting heavy ions. The number of nucleons exchanged between the two partners can be expressed as[33]

$$N_{ex} = \sigma_A^2 \tag{16}$$

At low energy dissipation σ_A^2 should depend approximately linearly on $\sqrt{T}$, the relative

velocity above the entrance channel Coulomb barrier, which is calculated as

$$\sqrt{T} = \sqrt{E_{cm} - V_c - TKEL}, \tag{17}$$

where E_{cm} is the initial center-of-mass kinetic energy, V_c is the Coulomb energy in the spherical nuclei approximation, and TKEL is the total kinetic energy loss. In this presentation, the physical range of $\sqrt{T}$ is limited by the entrance channel value of V_c - E_{cm}.

A linear dependence of $\sqrt{T}$ on σ_A^2 is an indication of the proportionality between the number of exchanges and the energy dissipated, thus supporting the idea of using nucleon exchange as means for energy dissipation. A plot of $\sqrt{T}$ as a function of σ_A^2 is shown in Figure 9 for the 672-MeV ^{56}Fe on ^{165}Ho system (diamonds) and the 840-MeV ^{56}Fe on ^{238}U system (circles). In both cases linear fits of $\sqrt{T}$ as a function of σ_A^2 are shown by the solid lines when all data points are included. In this case the slopes of $\sqrt{T}$ vs. σ_A^2 linear fits are nearly identical for both systems. This is not a surprising result since the initial relative velocities of the two systems are similar. However, a better fit of the data for the 672-MeV ^{56}Fe on ^{165}Ho system is obtained when the last two points, corresponding to high TKEL values, are excluded. The resulting fit is indicated by the dashed line. In this case the slope obtained is higher than that of the 840-MeV ^{56}Fe on ^{238}U system. The apparent linearity of $\sqrt{T}$ as a function of σ_A^2 obtained is consistent with the nucleon exchange mechanism description. Although this linearity does not exclude the possibility of other types of mechanisms, it shows that there is no sudden transition to a different mechanism in the region of energy loss presented.

8. SUMMARY

The projectile-like fragments obtained in the reaction ^{56}Fe on ^{165}Ho at 672 MeV have been measured, and the centroids <N>, and <Z>, variances, σ_Z^2 and σ_N^2, and correlation factors, ρ_{NZ} of their two-dimensional (N-Z) distribution were determined with the method of moment analysis. The evolution of <N>, <Z>, the $< N > / < Z >$ ratio, σ_Z^2, σ_N^2, and ρ_{NZ} as a function of total kinetic energy loss was described. A gradual decrease of

the experimental <N> and <Z> with increasing energy loss was observed. The determination of the primary distributions, by applying evaporation corrections to the secondary distributions, showed that the drift in <N> is mainly due to neutron evaporation, while the drift in <Z> is a consequence of the deep-inelastic mechanism[9]. The result is the formation of neutron-rich nuclei with N/Z ratios approaching the N/Z ratio of the composite system (1.38). This produces charge equilibration between the two reaction fragments without mass equilibration. A negative drift in the mass is found to be along the direction that would minimize the potential energy of the system and drive it towards mass asymmetry, for the 672-MeV ^{56}Fe on ^{165}Ho and the 840-MeV ^{56}Fe on ^{238}U systems.

The predictions of two nucleon exchange models, Randrup's model and Tassan-Got's model, were compared to the experimental data for Fe-induced reactions. Both models reproduce the experimental neutron and charge centroids, and the N/Z ratio for the 672-MeV ^{56}Fe on ^{165}Ho system. Significant differences between the predictions of the two models are observed for the 840-MeV ^{56}Fe on ^{238}U system. Tassan-Got's model reproduces the charge and neutron centroids quite well, while Randrup's model overpredicts both the neutron and proton centroids. It is interesting to point out that the N/Z ratio is equally well reproduced by both models, for all the systems studied here, despite their differences in the prediction of the individual neutron and proton centroids. An examination of the primary distributions obtained from the two models shows that the means to charge equilibration is by driving the system to mass symmetry in Randrup's model, and to mass asymmetry in Tassan-Got's model. Hence, Tassan-Got's model better reproduces the experimental results for systems with a greater mass asymmetry.

An increase in the experimental charge and neutron variances (σ_Z^2 and σ_N^2) with increasing energy loss was observed. This, in addition to the approximately linear dependence between $\sqrt{T}$ and σ_A^2, supports the role of nucleon exchange in energy dissipation. The variances and the correlation factor are equally well reproduced by both nucleon exchange models for the asymmetric systems studied, and nucleon exchange could account for most of the energy dissipation in the Fe-induced reactions presented here.

ACKNOWLEDGMENTS

The authors wish to thank L. Tassan-Got and J. Randrup for providing the computer codes based on their models, and C. Merouane for providing the data for the 840-MeV ^{56}Fe on ^{238}U system. This research was supported by the U.S. Department of Energy under Grants No. DEFG05-87ER40321 and No. DEFG02-93ER40802.

REFERENCES

1. M. Lefort and C.H. Ngö, Ann. Phys. **V. 3**, # 1 (1978).

2. A. Gobbi and W. Nörenberg, Heavy Ion Collisions, **Vol. 2**, R. Bock ed. (North-Holland, Amsterdam, 1980), p. 127.

3. H. Freiesleben and J. V. Kratz, *Phys. Rep.* 106, 1 (1984).

4. W.U. Schröder, and J.R. Huizenga, *Treatise on Heavy-Ion Science*, D.A. Bromley ed. (Plenum: New York, 1984), **Vol. 2**, p. 115.

5. B. Borderie, M.F. Rivet, and L. Tassan-Got, *Ann. Phys.* **15**, 287 (1990).

6. D.R. Benton, H. Breuer, F. Khazaie, K. Kwiatkowski, V.E. Viola, S. Bradley, A.C. Mignerey, and A.P. Weston-Dawkes, *Phys. Lett. B* **185**, 326 (1987), *Phys. Rev. C* **38**, 1207 (1988).

7. K. Kwiatkowski, R. Planeta, S. H. Zhou, V. E. Viola, H. Breuer, M. A. McMahan, A. C. Mignerey, *Phys. Rev. C* **41**, 958 (1990).

8. V. Penumetcha, G.A. Petitt, T.C. Awes, J.R. Beene, R.L. Ferguson, F.E. Obenshain, F. Plasil, G.R. Young, and S.P. Sorensen, *Phys. Rev. C* **42** 1489 (1990).

9. H. Madani Ph. D. Thesis PP # ER/40321-11; Univeristy of Maryland (1993).

10. H. Madani, A.C. Mignerey, and A.A. Marchetti, "Deep-Inelastic Reactions", Proceedings of the 9th Winter Workshop in Nuclear Dynamics: Advances in Nuclear Dynamics, Key West, Florida, U.S.A. January 30-February 6, 1993,.editors: B. Back, W. Bauer, and J. Harris, World Scientific, Singapore, 1993, p. 166.

11. R. Planeta, K. Kwiatkowski, S. W. Zhou, V. E. Viola, H. Breuer, M. A. McMahan, W. Kehoe, and A. C. Mignerey, *Phys. Rev. C* **41**, 942 (1990).

12. T. C. Awes, R. L. Ferguson, R. Novotny, F. E. Obenshain, F. Plasil, S. Pontoppidan, V. Rauch, G.R. Young, and H. Sann, *Phys. Rev. Lett.* **52**, 251 (1984).

13. H. Breuer, A. C. Mignerey, V. E. Viola, K.L. Wolf, J.R. Birkelund, D. Hilscher, J.R. Huizenga, W.U. Schröer, and W.W. Wilcke, *Phys. Rev. C* **28**, 1080 (1983).

14. D. R. Benton, Ph. D. Thesis PP # 86-030; University of Maryland (1985).

15. J. Randrup, *Ann. Phys.* (NY) 112, 356 (1978), *Nucl. Phys.* **A307**, 319 (1978), *Nucl. Phys.* **A327**, 490 (1979), *Nucl. Phys.* **A383**, 468 (1982).

16. L. Tassan-Got and C. Stephan, Internal Report INPO-DRE-89- 46, 1989. *Nucl. Phys.* **A524**, 121 (1991).

17. L. Tassan-Got, Ph.D. Thesis, INPO- T-89-02; Orsay, France, 1988.

18. A.A. Marchetti, A.C. Mignerey, H. Madani A. Gökmen, W.L. Kehoe, B. Libby, K. Morley, H. Breuer, K. Wolf, and F. Obenshain, *Phys. Rev. C* **48** 266 (1993).

19. H.C. Britt, B.H. Erkkila, A. Gavron, Y.Patin, R.H. Stokes, M.P.Webb, P.R. Christensen, Ole Hansen, S. Pontoppidan, F. Videbaek, R.L. Ferguson, F. Plasil, G.R. Young, and J. Randrup, *Phys. Rev. C* **26**, 1999 (1982).

20. H. Madani, A.A. Marchetti, and A.C. Mignerey, "Comparison of Mass and Charge Distributions to Model Predictions in Deep-Inelastic Reactions", Proceedings of the 8th Winter Workshop in Nuclear Dynamics: Advances in Nuclear Dynamics, Jackson Hole, Wyoming, U.S.A. January 19-25, 1992,.editors: W. Bauer and B. Back, World Scientific, Singapore, 1992, p. 32.

21. Computer Handbook of the Holifield Heavy-Ion Research Facility; Oak Ridge National Laboratory, Oak Ridge, Tennessee, 1987.

22. A. A. Marchetti and A. C. Mignerey, Nucl. Instrum. and Methods A **324**, 288 (1993).

23. A. Gavron, *Phys. Rev. C* **21**, 230 (1980).

24. D.K. Lock, R. Vandenbosch, and J. Randrup, *Phys. Rev. C* **31**, 1268 (1985).

25. H. Breuer,N.R. Yoder, A.C. Mignerey, K. Kwiatkowski, and K.L. Wolf, *Nucl. Instrum. and Methods* **204**, 419 (1983).

26. D. Hilsher, J.R. Birkelund, A.D. Hoover, W.U. Shcröeder, W.W. Wilker, J.R. Huizenga, A.C. Mignerey, K.L. Wolf, H. Breuer, and V.E. Viola, jr., *Phys. Rev. C* **20**, 576 (1979).

27. C. Merouane, Ph. D. Thesis. # ORO-5172-0026 University of Maryland (1986).

28. W.J. Myers and W.J. Swiatecki, *Ark. Phys.* **36**, 343 (1967).

29. L. G. Moretto, *Zeit. Phys. A* **310**, 61 (1983).

30. J. J. Griffin, J. A. Lukasiak, M. Dworzecka, *Zeit. Phys. A* **326**, 51 (1987).

31. E.J. Garcia-Solis, H. Madani, A.C. Mignerey, A.A. Marchetti, and D.E. Russ (to be published).

32. P.L. Gonthier, P. Harper, B. Bouma, R. Ramaker, D.A. Cebra, Z.M. Koening, D. Fox, and G.D. Westfall, *Phys. Rev. C* **41**, 2635 (1990).

33. W. U. Schröeder and J. R. Huizenga, *Ann. Rev. Nucl. Sci.* **27**, 465 (1977).

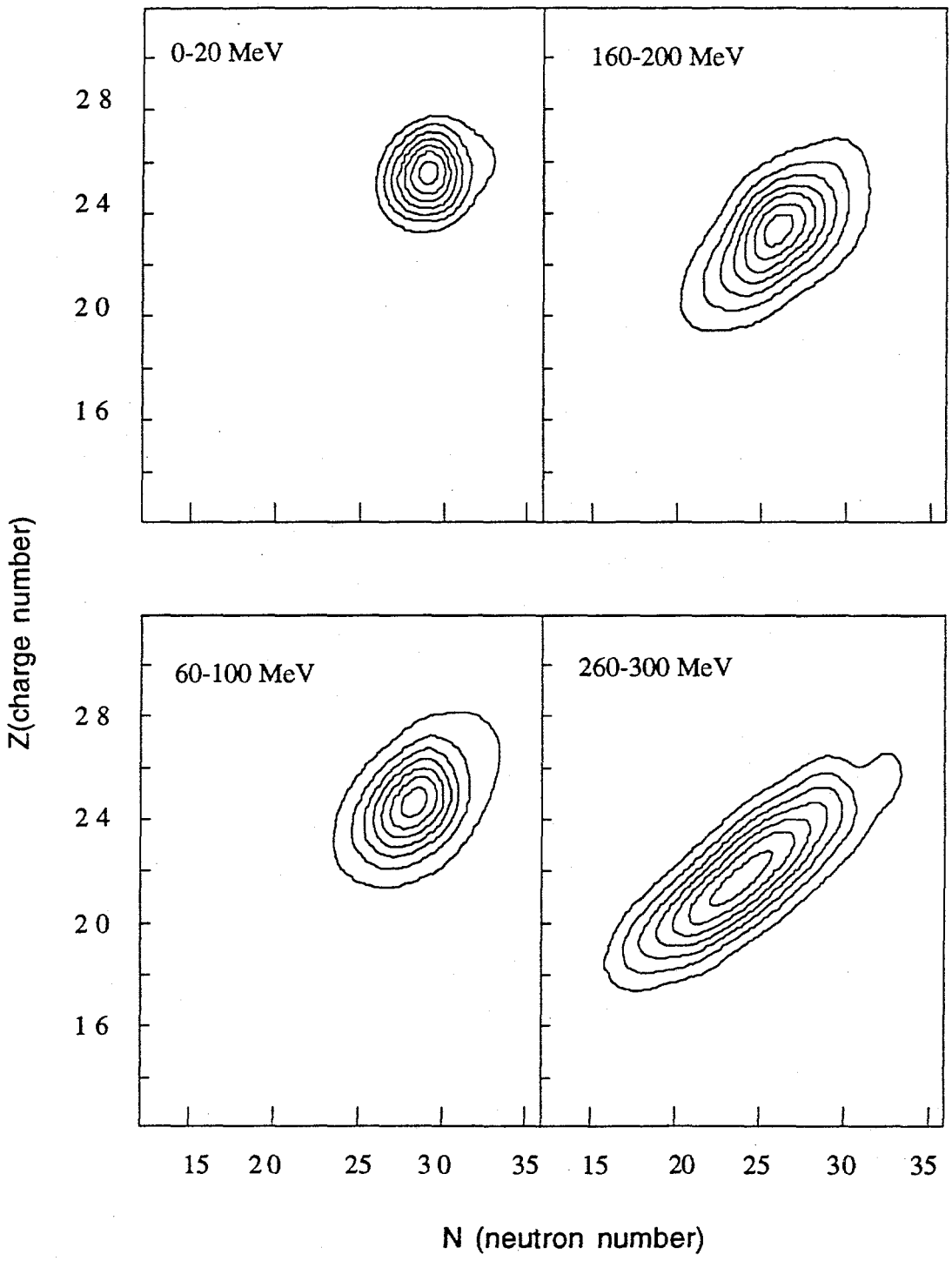

Figure 1. Contour lines of the measured yield in the N-Z plane obtained with the reaction $^{56}Fe + ^{165}Ho$ at 672 MeV for four representative bins of TKEL. The lines indicate events with 90%, 70%, 50%, 30%, 10% of the maximum yield of each distribution.

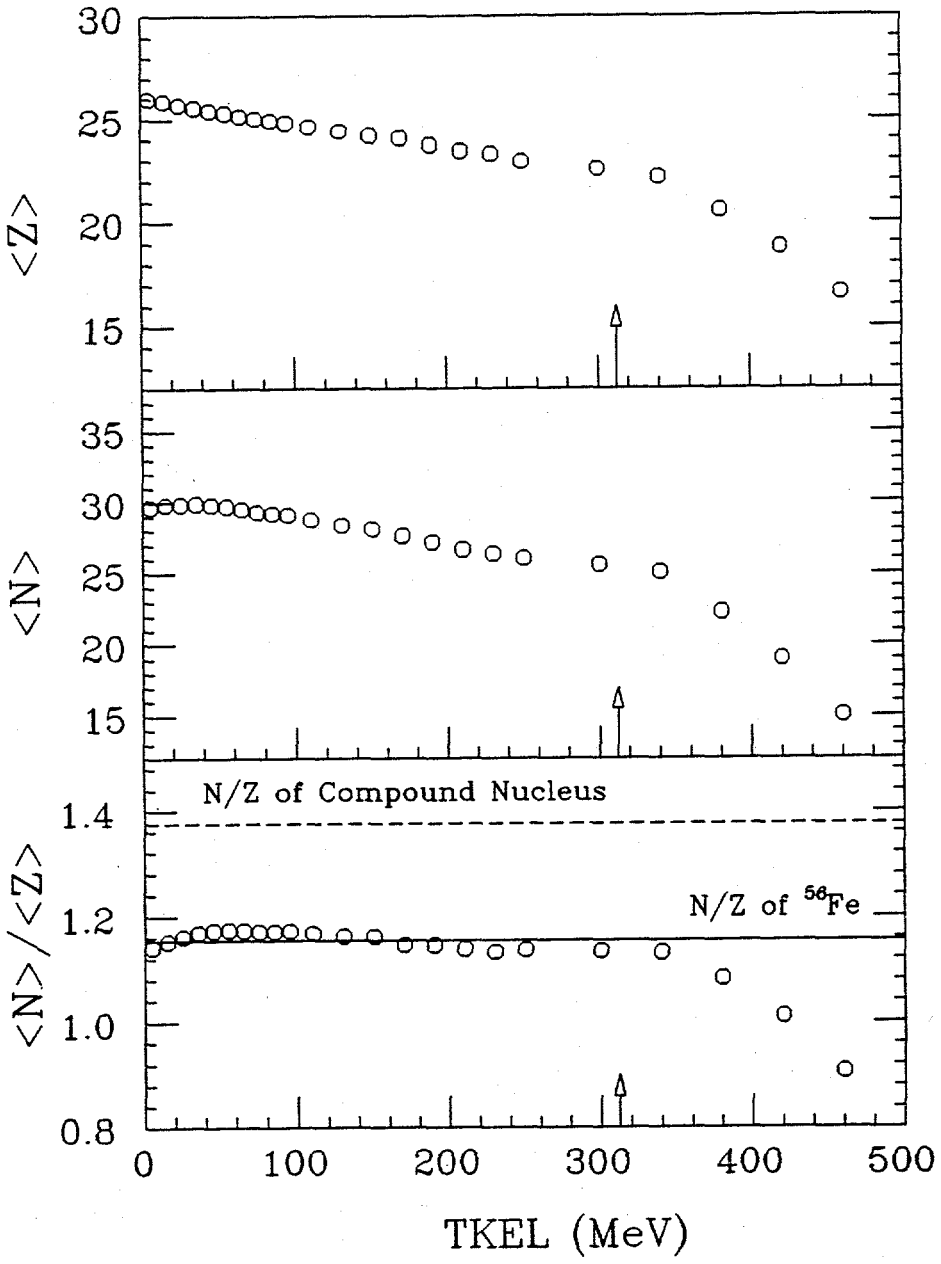

Figure 2.The <N>, <Z>, and <N>/<Z> ratio as a function of total kinetic energy loss TKEL for the 672-MeV ^{56}Fe + ^{165}Ho reaction. The TKEL scale is corrected for evaporation effects assuming an equipartition of the excitation energy between the reaction fragments. The solid and dashed lines indicate the N/Z ratio of the projectile and composite system, respectively. The arrow indicates the limit imposed by the entrance channel Coulomb barrier.

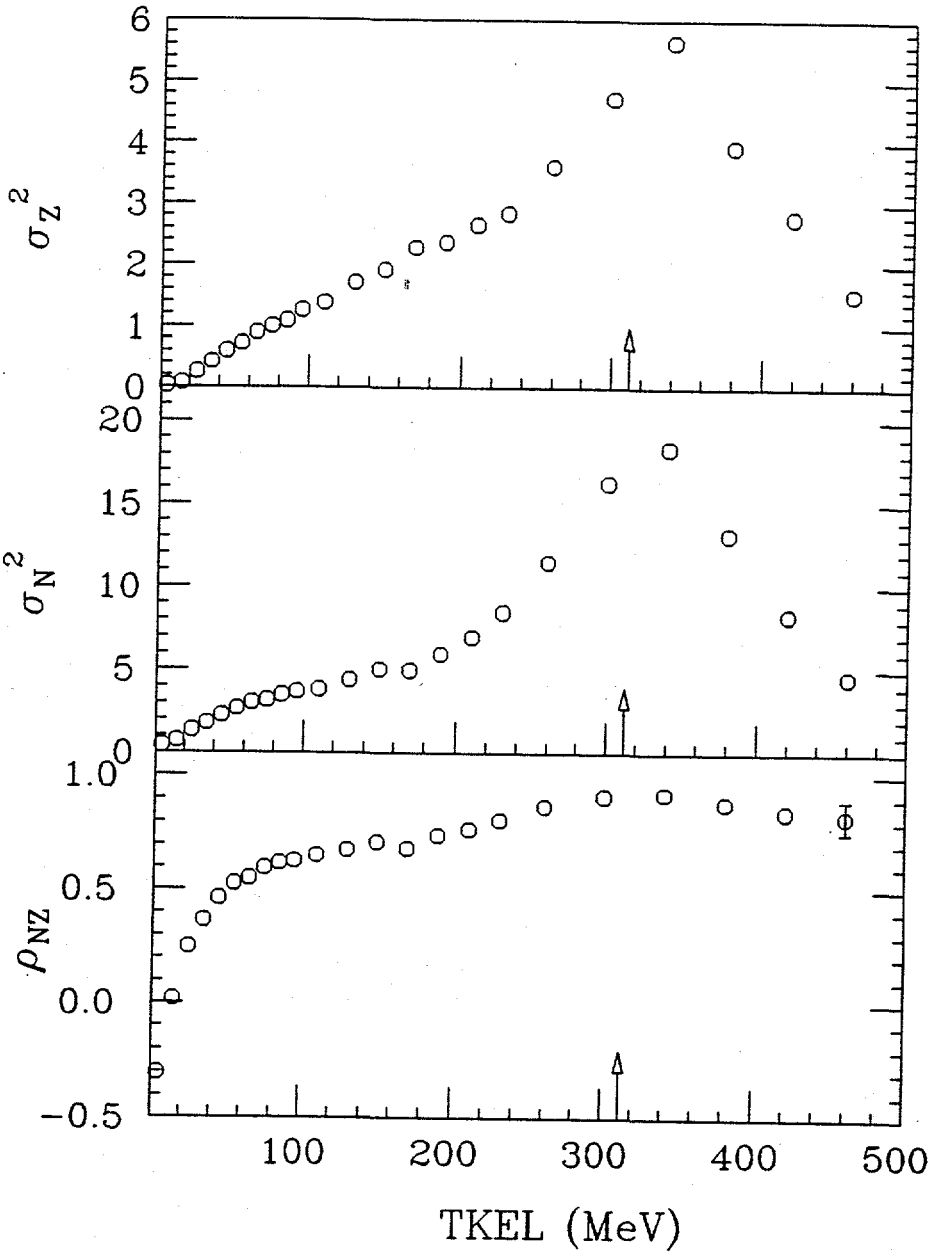

Figure 3. The variances σ_Z^2 and σ_N^2, and the correlation factor ρ_{NZ} as a function of TKEL for the 672-MeV ^{56}Fe + ^{165}Ho reaction. The TKEL scale is corrected for evaporation effects assuming an equipartition of the excitation energy between the reaction fragments. The arrow indicates the limit imposed by the entrance channel Coulomb barrier.

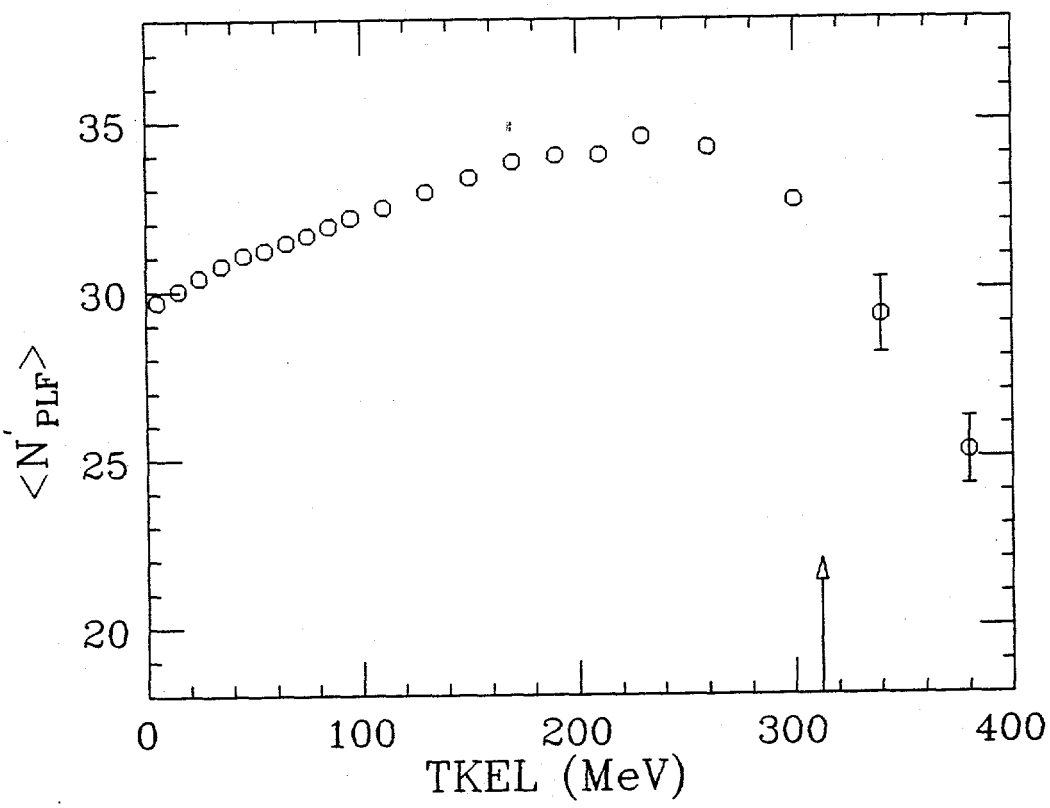

Figure 4. The primary centroids, $\langle N'_{PLF} \rangle$, as a function of TKEL for the 672-MeV ^{56}Fe + ^{165}Ho reaction. The arrow indicates the limit imposed by the entrance channel Coulomb barrier.

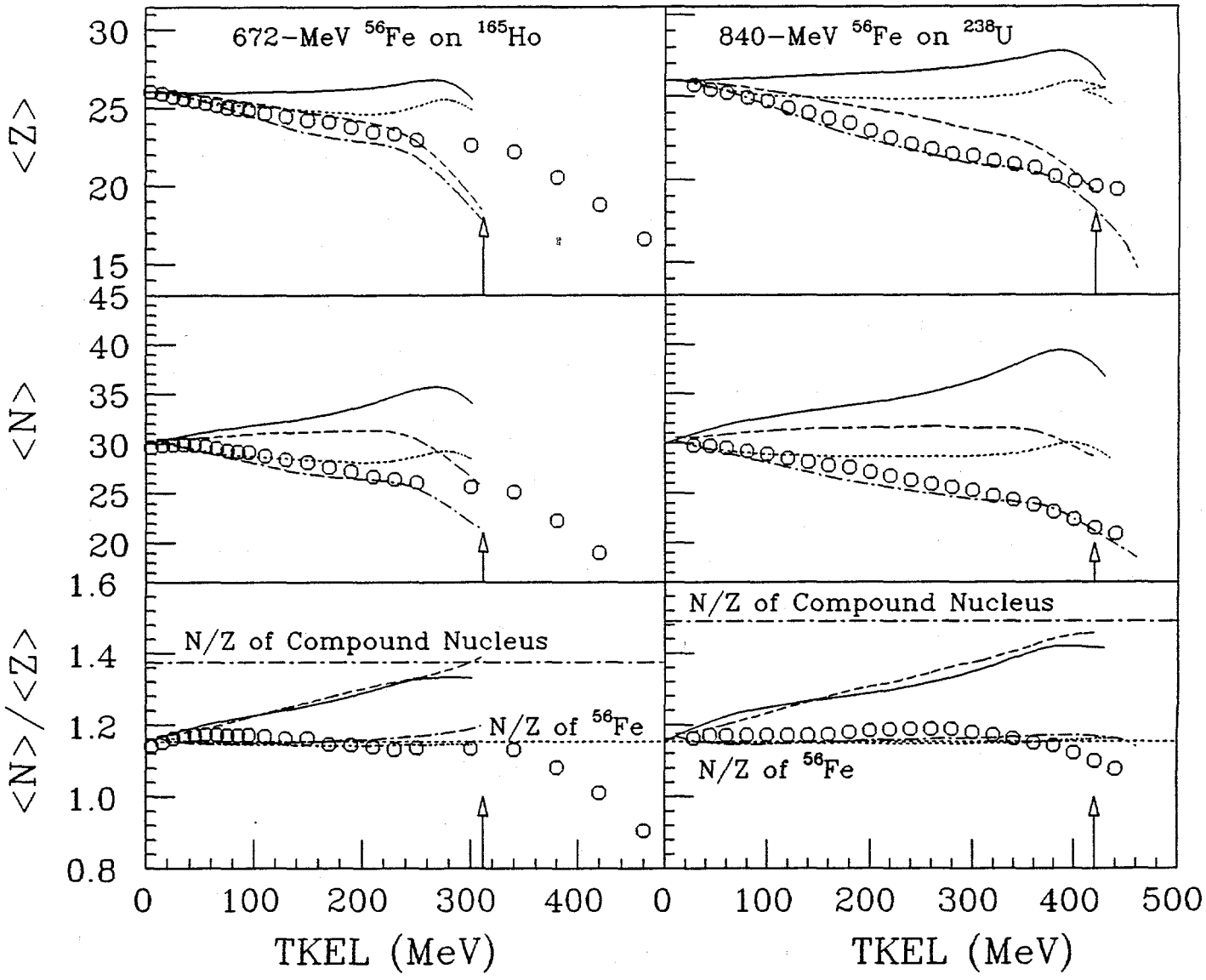

Figure 5.Experimental data and model predictions for <N>, <Z>, and <N>/<Z> of the nuclide distributions obtained in the 672-MeV ^{56}Fe on ^{165}Ho and the 840-MeV ^{56}Fe on ^{238}U reactions as a function of TKEL. The solid and dotted lines refer to Randrup's model predictions before and after evaporation corrections, respectively. Similarly, the dashed and dot-dashed lines refer to Tassan-Got's model predictions before and after evaporation corrections, respectively. The N/Z ratio of the compound nucleus and the projectile are indicated by the dot-dashed and dotted lines, respectively.

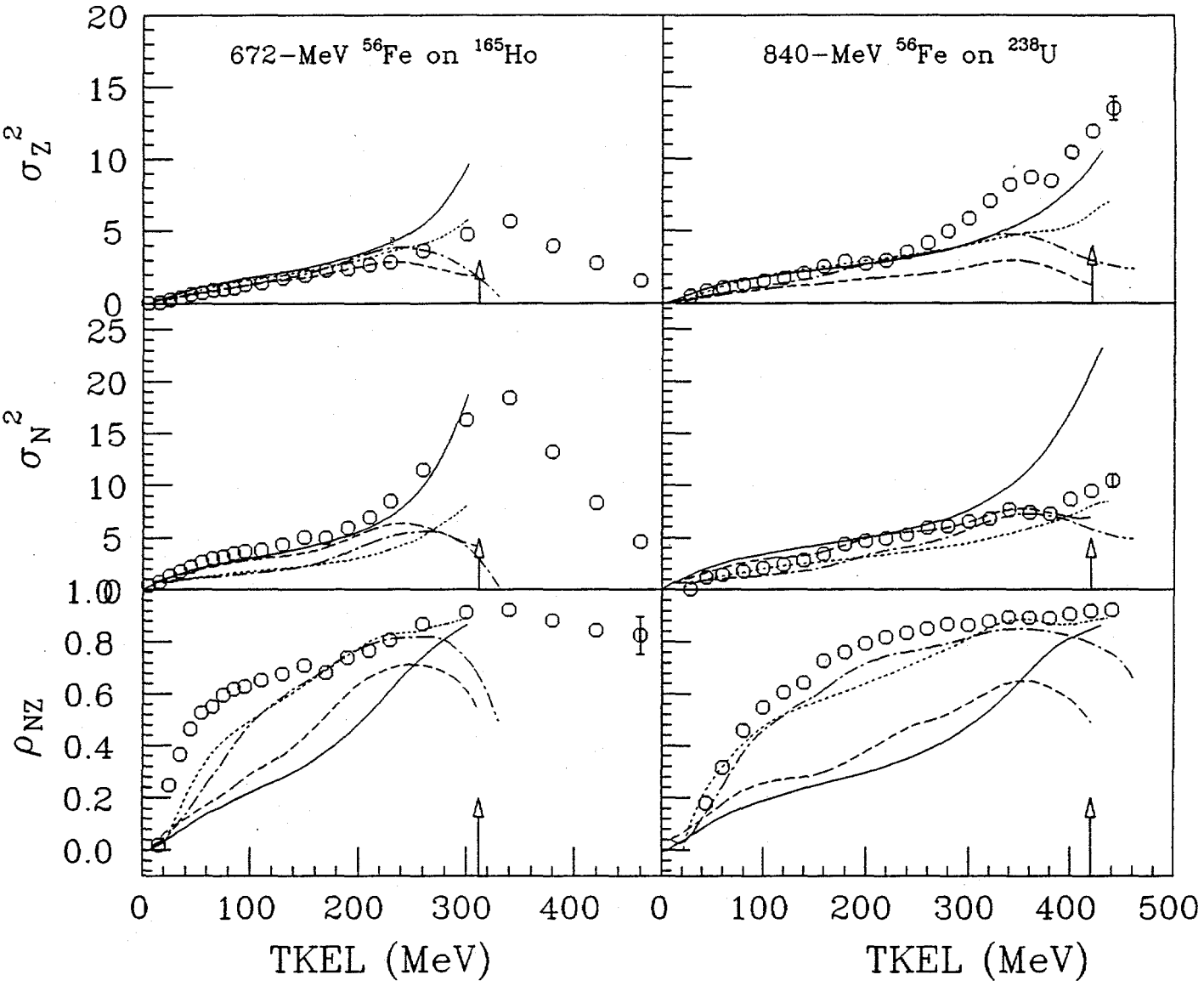

Figure 6. Experimental data and model predictions for σ_Z^2, σ_N^2, and ρ_{NZ} of the nuclide distributions obtained in the 672-MeV ^{56}Fe on ^{165}Ho and the 840-MeV ^{56}Fe on ^{238}U reactions as a function of TKEL. The solid and dotted lines refer to Randrup's model predictions before and after evaporation corrections, respectively. Similarly, the dashed and dot-dashed lines refer to Tassan-Got's model predictions before and after evaporation corrections, respectively. The N/Z ratio of the compound nucleus and the projectile are indicated by the dot-dashed and dotted lines, respectively.

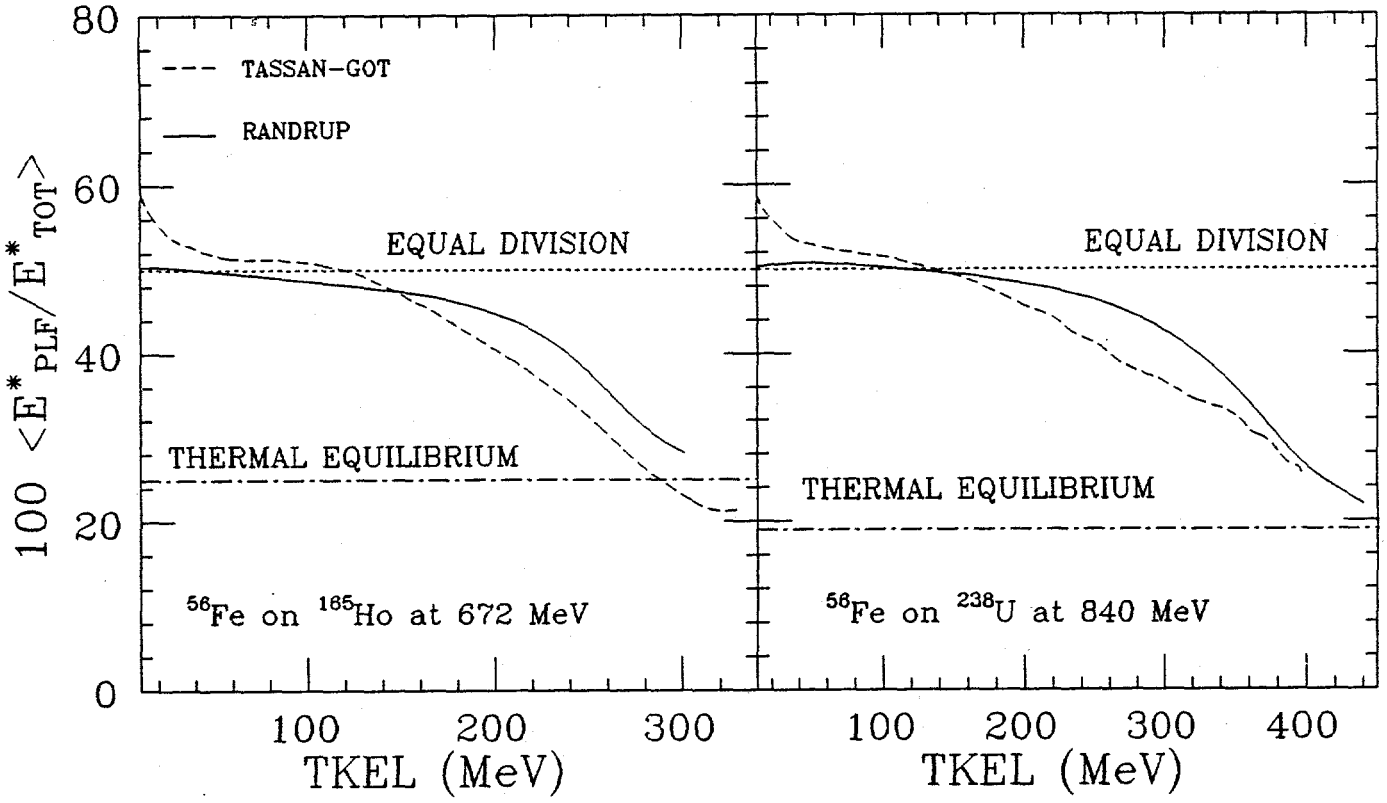

Figure 7. The ratio of excitation energy stored in the projectile-like fragments produced by the 672-MeV ^{56}Fe on ^{165}Ho reaction. The solid line refers to Randrup's model calculations, and the dashed line refers to Tassan-Got's model calculations. The limits of equipartition of the excitation energy and thermal equilibrium between the two reaction partners are indicated by the dotted and the dot-dashed lines, respectively.

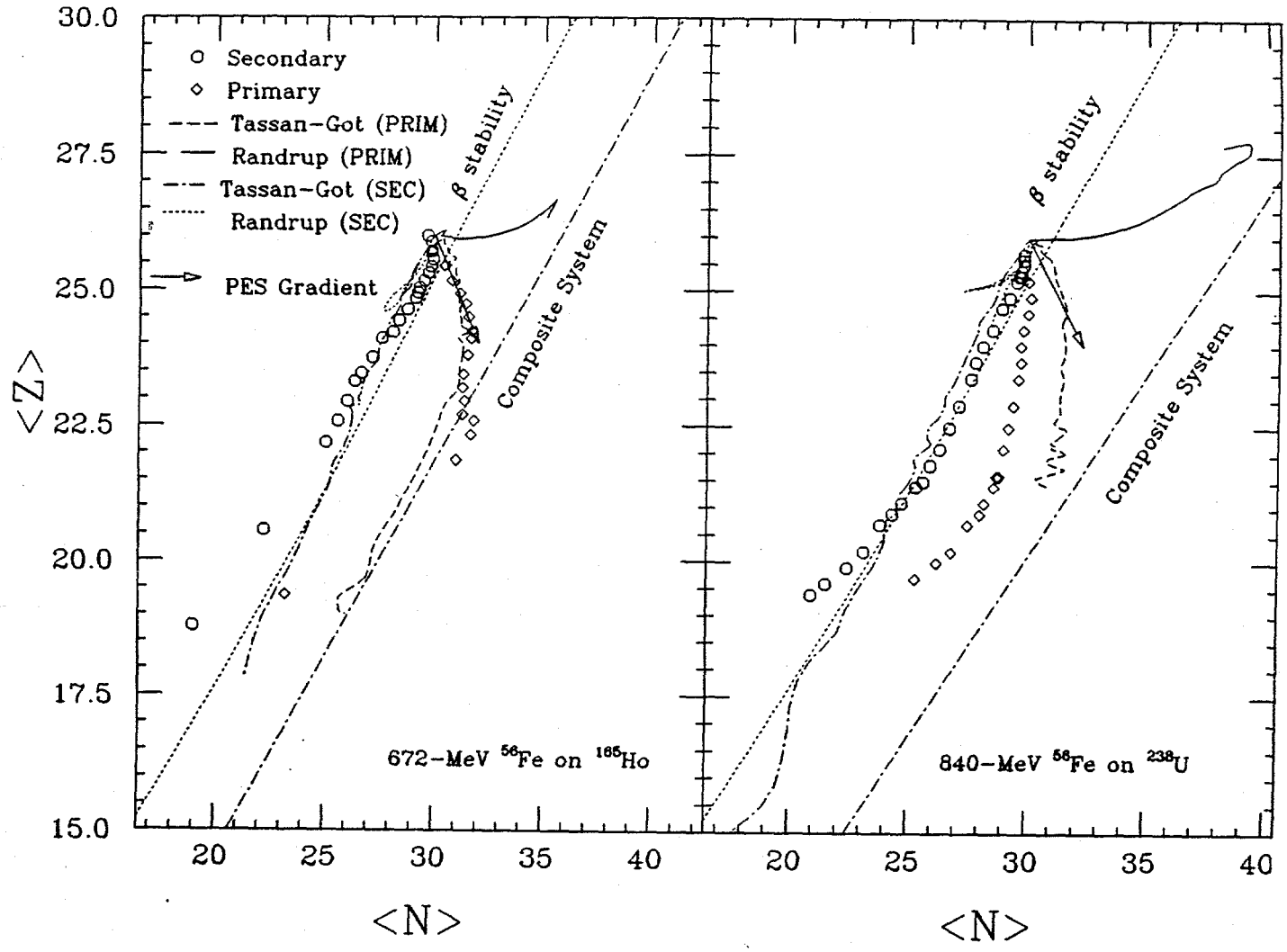

Figure 8. Evolution of the nuclide distribution in the N-Z plane of the projectile-like fragments produced in the 672-MeV ^{56}Fe on ^{165}Ho and the 840-MeV ^{56}Fe on ^{238}U reactions, as a function of energy loss. The experimental distributions are indicated by the circles for secondary fragments and diamonds for primary fragments. The primary distributions predicted by Randrup's model and Tassan-Got's model are indicated by the solid and dashed lines, respectively. The calculated secondary distributions are indicated by the dot-dashed and dotted lines for Tassan-Got's model and Randrup's model, respectively. The PES gradient at the injection point is shown by the arrow.

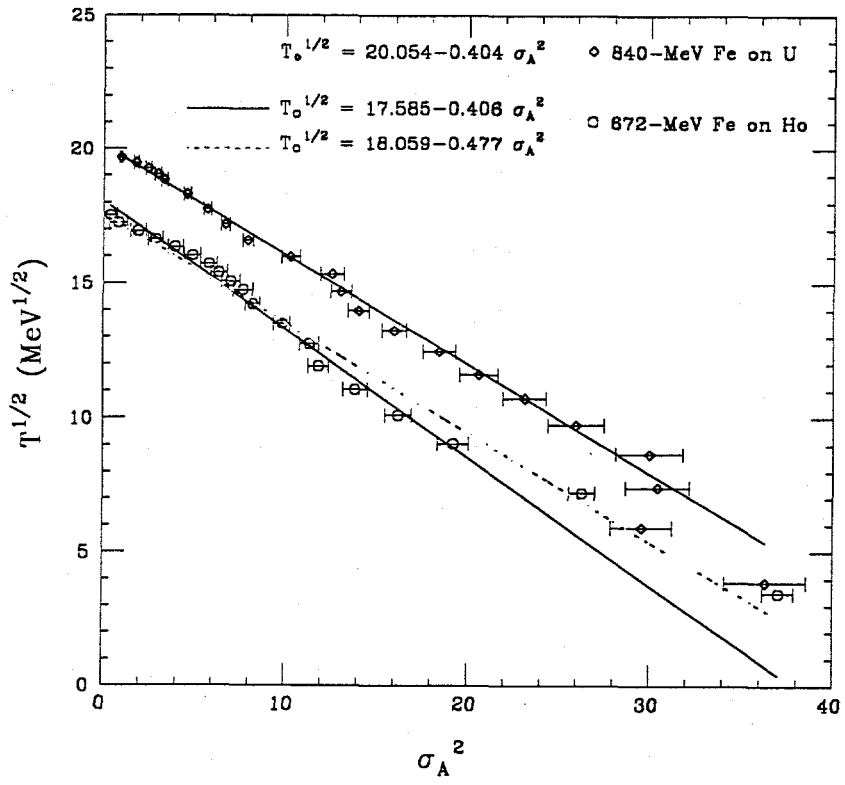

Figure 9. The square root of the available kinetic energy above the entrance channel Coulomb barrier $\sqrt{T}$ as a function of σ_A^2 for the 672-MeV ^{56}Fe on ^{165}Ho and the 840-MeV ^{56}Fe on ^{238}U reactions indicated by the circles and diamonds, respectively. The 840-MeV ^{56}Fe on ^{238}U data are from Ref. 26.

Table 1. The secondary $< N >$ and $< Z >$ for the ^{56}Fe on ^{165}Ho reaction at 672 MeV. The TKEL scale has been corrected for evaporation assuming equal excitation energy division.

TKEL (MeV)	$< Z >$	$< N >$
5	26.00 ± 0.01	29.65 ± 0.01
15	25.89 ± 0.01	29.83 ± 0.01
25	25.71 ± 0.02	29.86 ± 0.01
35	25.57 ± 0.02	29.89 ± 0.02
45	25.43 ± 0.02	29.82 ± 0.02
55	25.31 ± 0.03	29.72 ± 0.03
65	25.16 ± 0.03	29.51 ± 0.03
75	25.03 ± 0.03	29.31 ± 0.03
85	24.94 ± 0.04	29.21 ± 0.03
95	24.84 ± 0.04	29.12 ± 0.04
110	24.63 ± 0.04	28.76 ± 0.03
130	24.43 ± 0.04	28.38 ± 0.03
150	24.21 ± 0.05	28.11 ± 0.04
170	24.10 ± 0.05	27.62 ± 0.04
190	23.74 ± 0.06	27.18 ± 0.05
210	23.45 ± 0.06	26.67 ± 0.06
230	23.30 ± 0.05	26.37 ± 0.06
260	22.93 ± 0.05	26.04 ± 0.06
300	22.57 ± 0.06	25.60 ± 0.07
340	22.17 ± 0.06	25.07 ± 0.08
380	20.56 ± 0.07	22.25 ± 0.08
420	18.78 ± 0.07	18.99 ± 0.07
460	16.60 ± 0.09	15.04 ± 0.097

Table 2. The secondary σ_Z^2, σ_N^2, and ρ_{NZ} for the reaction ^{56}Fe + ^{165}Ho at 672 MeV. The TKEL scale has been corrected for evaporation assuming equal excitation energy division.

TKEL (MeV)	σ_Z^2	σ_N^2	ρ_{NZ}
5	0.031 ± 0.003	0.433 ± 0.005	-0.305 ± 0.013
15	0.073 ± 0.007	0.731 ± 0.014	0.019 ± 0.007
25	0.251 ± 0.017	1.342 ± 0.037	0.248 ± 0.016
35	0.419 ± 0.023	1.772 ± 0.054	0.365 ± 0.019
45	0.594 ± 0.028	2.244 ± 0.069	0.463 ± 0.021
55	0.721 ± 0.035	2.669 ± 0.086	0.527 ± 0.025
65	0.895 ± 0.041	3.046 ± 0.098	0.551 ± 0.025
75	1.002 ± 0.047	3.180 ± 0.107	0.596 ± 0.028
85	1.084 ± 0.050	3.485 ± 0.125	0.618 ± 0.029
95	1.264 ± 0.060	3.685 ± 0.135	0.628 ± 0.031
110	1.387 ± 0.048	3.818 ± 0.106	0.652 ± 0.023
130	1.719 ± 0.060	4.384 ± 0.134	0.677 ± 0.026
150	1.921 ± 0.072	5.018 ± 0.164	0.709 ± 0.029
170	2.282 ± 0.083	4.963 ± 0.182	0.682 ± 0.031
190	2.368 ± 0.097	5.936 ± 0.234	0.739 ± 0.036
210	2.652 ± 0.115	6.967 ± 0.283	0.767 ± 0.039
230	2.840 ± 0.133	8.449 ± 0.354	0.807 ± 0.043
260	3.613 ± 0.122	11.483 ± 0.348	0.868 ± 0.033
300	4.731 ± 0.148	16.277 ± 0.462	0.913 ± 0.032
340	5.654 ± 0.176	18.390 ± 0.540	0.924 ± 0.033
380	3.933 ± 0.150	13.204 ± 0.457	0.884 ± 0.038
420	2.780 ± 0.179	8.316 ± 0.398	0.845 ± 0.057

460	1.536 ± 0.137	4.597 ± 0.329	0.825 ± 0.072

Table 3. The primary neutron centroids, N'_{PLF}, obtained with neutron evaporation corrections, for the reaction $^{56}Fe + ^{165}Ho$ at 672 MeV.

TKEL (MeV)	$< N >$
5	29.70 ± 0.17
15	30.03 ± 0.38
25	30.40 ± 0.49
35	30.76 ± 0.54
45	31.05 ± 0.58
55	31.19 ± 0.63
65	31.43 ± 0.68
75	31.65 ± 0.71
85	31.90 ± 0.74
95	32.16 ± 0.80
110	32.44 ± 0.61
130	32.90 ± 0.68
150	33.33 ± 0.76
170	33.79 ± 0.81
190	33.98 ± 0.91
210	33.99 ± 1.00
230	34.54 ± 1.16
260	34.19 ± 0.97
300	32.62 ± 1.09
340	29.21 ± 1.10
380	25.20 ± 1.01